Single-Image Super-Resolution via an Iterative Reproducing Kernel Hilbert Space Method

Liang-Jian Deng, Weihong Guo, and Ting-Zhu Huang

Abstract—Image super-resolution (SR), a process to enhance image resolution, has important applications in satellite imaging, high-definition television, medical imaging, and so on. Many existing approaches use multiple low-resolution (LR) images to recover one high-resolution (HR) image. In this paper, we present an iterative scheme to solve *single*-image SR problems. It recovers a high-quality HR image from solely one LR image without using a training data set. We solve the problem from image intensity function estimation perspective and assume that the image contains smooth and edge components. We model the smooth components of an image using a thin-plate reproducing kernel Hilbert space and the edges using approximated Heaviside functions. The proposed method is applied to image patches, aiming to reduce computation and storage. Visual and quantitative comparisons with some competitive approaches show the effectiveness of the proposed method.

Index Terms—Heaviside function, iterative reproducing kernel Hilbert space (RKHS), single-image super-resolution (SR), thin-plate spline.

I. INTRODUCTION

IMAGE super-resolution (SR), a quite active research field currently, is a process to estimate a high-resolution (HR) image from one or multiple low-resolution (LR) images. HR means more details and better visibility. Due to limitation of hardware devices and high cost, one sometimes can collect only LR images. For instance, synthetic aperture radar and satellite imaging cannot get HR images due to long distance and air turbulence. In medical imaging magnetic resonance imaging (MRI), HR images need more time and cost [48], [61]. Thus, developing a more accurate and faster image SR algorithm is important and has a lot of applications.

L.-J. Deng and T.-Z. Huang are with the School of Mathematical Sciences, University of Electronic Science and Technology of China, Chengdu 611731, China (e-mail: liangjian1987112@126.com; tingzhuhuang@126.com).

W. Guo is with the Department of Mathematics, Applied Mathematics and Statistics, Case Western Reserve University, Cleveland, OH 44106 USA (e-mail: wxg49@case.edu).

Fig. 1. (a) LR image. (b) SR image using bicubic interpolation method (note the blur effect). (c) SR image by nearest neighbor interpolation method (note the jaggy effect on the edges). The upscaling factor is 4.

A. Literature Review

In this section, we review some existing SR methods, some of which will be compared with the proposed method.

Many existing image SR methods need multiple LR images as inputs. We refer to them as multiple-image SR. Mathematically, there are p LR images $y_i \in \mathbb{R}^m$ available, and y_i is related to an HR image $x \in \mathbb{R}^n$ by

$$y_i = DB_i x + n_i, \quad 1 \le i \le p \tag{1}$$

where $D \in \mathbb{R}^{m \times n}$ is a downsampling operator, $B_i \in \mathbb{R}^{n \times n}$ is a blurring operator that might happen due to, for instance, out of focus, and $n_i \in \mathbb{R}^m$ represents random noise [52].

This paper addresses single-image SR, i.e., $p = 1$ in (1). Compared with multiple-image SR, single-image SR is more applicable when there is only one LR image available. Obviously, it is also more challenging.

Existing SR methods, for both multiple images and single image, can be roughly put into several categories: interpolation based, statistics based, learning based, and others. This classification is by no means the best, but provides an organized way for literature review. Note that ideas of methods in different categories might have overlap. For instance, some learning-based methods might also involve statistics.

Interpolation is a straightforward idea for image SR. There are two popular classical interpolation methods: 1) nearest neighbor interpolation and 2) bicubic interpolation. Nearest neighbor interpolation fills in intensity at an unknown location by that of its nearest neighbor point. It often causes jaggy effect [see Fig. 1(c)]. Bicubic interpolation is to utilize a cubic kernel to interpolate. It tends to create blur effect [see Fig. 1(b)]. Recently, some state-of-the-art interpolation methods have been proposed [26], [27], [40], [45], [65], [66], [70]. In [40], for instance, it presents a new edge-directed

interpolation method. It estimates local covariance coefficients from an LR image, and then applies the coefficients to interpolate an HR image. In [74], the proposed edge-guided nonlinear interpolation is based on directional filtering and data fusion. It can preserve sharp edges and reduce ring artifacts. Mueller *et al.* [45] proposed an interpolation algorithm using contourlet transform and wavelet-based linear interpolation scheme. The proposed method belongs to this category.

Maximum *a posteriori* and maximum likelihood estimator are popular statistics-based methods [6], [19], [20]. To preserve sharp edges, Fattal [20] utilized statistical edge dependency to relate edge features in LR and HR images. Farsiu *et al.* [19] proposed an alternate approach using L_1-norm minimization and a bilateral prior-based robust regularization.

Learning-based approaches are a powerful tool for image SR [10], [21], [23]–[25], [30], [37], [38], [41], [55], [56], [58], [60], [69], [76]. They normally start from two large training data sets, one formed of LR images and the other formed of HR images, and then learn a relation between LR and HR images. The relation is then applied to a given LR image to get an HR image. Learning-based methods usually can obtain high-quality images, but they are computationally expensive. The results might depend on the selection of training data. In addition, they are not a completely single-image SR since two large data sets are required for learning. Sun *et al.* [56] utilized sketch priors to extend the low vision learning approach in [25] to get clear edges, ridges, and corners. Sun *et al.* [55] proposed a novel profile prior of image gradient, which can describe the shape and the sharpness of an image to obtain SR images. Qinlan *et al.* [69] proposed a method via an example-based strategy that divides the high-frequency patches of an LR image into different classes. This method can accelerate image SR procedure. Fernandez-Granda and Candès [21] used transform-invariant group-sparse regularization. This method performs well for highly structured straight edges and high upscaling factors. In recent years, sparsity methods, usually associated with learning-based ideas, have been widely discussed for image SR [15], [33], [70]–[73], [75]. Yang *et al.* [71], [72] utilized sparse signal representation to develop a novel method for single-image SR. They first sought a sparse representation for each patch of the LR image and computed corresponding coefficients, and then generated the HR image via the computed coefficients. Recently, Zeyde *et al.* [73] proposed a local sparse-land model on image patches based on [71] and [72] and obtained improved results.

In addition, many other image SR methods have also been proposed, e.g., a frequency technique [3], pixel classification methods [1], [2], iterative back projection methods [11], [34], [39], [57], a hybrid method [14], a kernel regression method [59], and others [5], [9], [22], [53], [62].

In summary, single-image SR is still a challenging problem. Existing single-image SR methods either need training data sets and expensive computation or lead to blur or jaggy effects. The aim of this paper is to use a simple mathematical scheme to recover a high-quality HR image from one LR image.

B. Motivation and Contributions of the Proposed Work

In this paper, we use reproducing kernel Hilbert space (RKHS) and Heaviside functions to study single-image SR with only one LR image as an input. We cast the SR problem as an image intensity function estimation problem. Since images contain edges and smooth components, we model them separately. We assume that the smooth components belong to a special Hilbert space called RKHS that can be spanned by a basis. We model the edges using a set of Heaviside functions. We then use intensity information of the given LR image defined on a coarser grid to estimate coefficients of the basis and redundant functions, and then utilize the coefficients to generate HR images at any finer grids. For even better performance, we make the procedure iterative to recover more details, motivated by the iterative back projection method [34] and the iterative regularization method [47].

This paper has the following main contributions.

1) To the best of our knowledge, this is the first work to employ RKHS method to get competitive image SR results. RKHS-based methods have been considered as a powerful tool to address machine learning for a long time. In image processing, however, only limited studies have been done, e.g., image denoising [4], image segmentation [36], and image colorization [49].

2) Employing Heaviside functions to recover more image details, not only getting sharp image edges but also preserving more high-frequency details on nonedge regions.

C. Organization of This Paper

The organization of this paper is as follows. In Section II, we review RKHS and splines-based RKHS. We will also make two remarks in this section. In Section III, we present the proposed iterative RKHS model based on Heaviside functions and discuss the algorithms. Many visual and quantitative experiments are shown in Section IV to demonstrate that the proposed method is a competitive approach for single-image SR. Finally, we draw the conclusions in Section V.

II. REVIEW ON SPLINES-BASED RKHS

In this section, we review RKHS, splines-based RKHS [63], and their applications in signal/image smoothing. We will use splines-based RKHS to model the smooth components of images.

A. Review on RKHS and Its Applications

Given a subset $\mathcal{X} \subset \mathbb{R}$ and a probability measure $\mathbb{P}$ on $\mathcal{X}$, we consider a Hilbert space $\mathcal{H} \subset L^2(\mathbb{P})$, a family of functions $g : \mathcal{X} \rightarrow \mathbb{R}$, with $\|g\|_{L^2(\mathbb{P})} < \infty$, and an associated inner product $\langle \cdot, \cdot \rangle_{\mathcal{H}}$ under which $\mathcal{H}$ is complete. The space $\mathcal{H}$ is an RKHS, if there exists a symmetric function $\mathbb{K} : \mathcal{X} \times \mathcal{X} \rightarrow \mathbb{R}$ such that: 1) for each $x \in \mathcal{X}$, the function $\mathbb{K}(\cdot, x)$ belongs to Hilbert space $\mathcal{H}$ and 2) there exists reproducing relation $f(x) = \langle f, \mathbb{K}(\cdot, x) \rangle_{\mathcal{H}}$ for all $f \in \mathcal{H}$. Any such symmetric kernel function must be positive semidefinite (see Definition 1). Under suitable regularity conditions, Mercer's theorem [43] guarantees that

the kernel has an eigenexpansion of the form $\mathbb{K}(x, x') = \sum_{k=1}^{\infty} \lambda_k \phi_k(x)\phi_k(x')$, with $\lambda_1 \geq \lambda_2 \geq \lambda_3 \geq \cdots \geq 0$ being a nonnegative sequence of eigenvalues, and $\{\phi_k\}_{k=1}^{\infty}$ associated eigenfunctions, taken to be orthonormal in $L^2(\mathbb{P})$.

Definition 1 (Positive Semidefinite Kernel): Let $\mathcal{X}$ be a nonempty set. The kernel $\mathbb{K} : \mathcal{X} \times \mathcal{X} \to \mathbb{R}$ is positive semidefinite if and only if Gram matrix $K = [\mathbb{K}(x_i, x_j)]_{N \times N}$, $x_i \in \mathcal{X}, i, j = 1, 2, \ldots, N$, is a positive semidefinite matrix.

Since the eigenfunctions $\{\phi_k\}_{k=1}^{\infty}$ form an orthonormal basis, any function $f \in \mathcal{H}$ has an expansion of the form $f(x) = \sum_{k=1}^{\infty} \sqrt{\lambda_k} a_k \phi_k(x)$, where $a_k = \langle f, \phi_k \rangle_{L^2(\mathbb{P})} = \int_{\mathcal{X}} f(x)\phi_k(x) \, d\mathbb{P}(x)$ are (generalized) Fourier coefficients. Let $f = \sum \ldots$ and $g = \sum \ldots$ be two functions in H. There are two distinct inner products. The first is the usual inner product in the space $L^2(\mathbb{P})$ defined as $\langle f, g \rangle_{L^2(\mathbb{P})} := \int_{\mathcal{X}} f(x)g(x) \, d\mathbb{P}(x) = \sum_{k=1}^{\infty} \lambda_k a_k b_k$ by Parseval's theorem. The second inner product, denoted by $\langle f, g \rangle_{\mathcal{H}}$, defines the Hilbert space. It can be written in terms of the kernel eigenvalues and generalized Fourier coefficients as $\langle f, g \rangle_{\mathcal{H}} = \sum_{k=1}^{\infty} a_k b_k$. Using this definition, the Hilbert ball of radius 1 for $\mathcal{H}$ with eigenvalues λ_k and eigenfunctions $\phi_k(\cdot)$ is $\mathbb{B}_{\mathcal{H}}(1) = \{f \in \mathcal{H}; \ f(\cdot) = \sum_{k=1}^{\infty} \sqrt{\lambda_k} b_k \phi_k(\cdot) \mid \sum_{k=1}^{\infty} b_k^2 = \|b\|_2^2 \leq 1\}$. The class of RKHS contains many interesting classes that are widely used in practice including polynomials of degree d ($\mathbb{K}(x, y) = (1 + \langle x, y \rangle)^d$), Sobolev spaces with smoothness v, Lipschitz, and smoothing splines. Moreover, kernel $\mathbb{K}(x, x') = (1/2)e^{-\gamma|x-x'|}$ leads to Sobolev space $\mathcal{H}_1$, i.e., a space consisted of square-integrable functions whose first-order derivative is square integrable. $\mathbb{K}(x, x') \propto |x - x'|$ and $\mathbb{K}(x, x') \propto |x - x'|^3$ correspond to 1D piecewise linear and cubic splines, respectively.

RKHS has appeared for many years, and it has been used as a powerful tool for machine learning [7], [8], [12], [13], [44], [46], [50], [54], [63]. Its application in image processing is not so common yet. Bouboulis *et al.* [4] proposed an adaptive kernel method to deal with image denoising problem in the spatial domain. This method can remove many kinds of noises (e.g., Gaussian noise, impulse noise, and mixed noise) and preserve image edges effectively. In addition, Kang *et al.* [36] and Quang *et al.* [49] utilized RKHS method to do image segmentation and image/video colorization, respectively.

Wahba [63] proposed splines-based RKHS for smoothing problems. It shows that the solution to an optimization problem consists of a set of polynomial splines. The proposed method is based on splines-based RKHS. We thus review them in the following sections.

B. 1D Spline and Signal Smoothing

For a real-valued function

$$f \in \mathcal{G} = \{f : f \in \mathcal{C}^{m-1}[0, 1], f^{(m)} \in \mathcal{L}_2[0, 1]\}$$

it can be expanded at $t = 0$ by Taylor series as

$$f(t) = \sum_{v=0}^{m-1} \frac{t^v}{v!} f^{(v)}(0) + \int_0^1 \frac{(t-u)_+^{m-1}}{(m-1)!} f^{(m)}(u)du$$

$$= f_0(t) + f_1(t) \tag{2}$$

with

$$f_0(t) = \sum_{v=0}^{m-1} \frac{t^v}{v!} f^{(v)}(0)$$

and

$$f_1(t) = \int_0^1 \frac{(t-u)_+^{m-1}}{(m-1)!} f^{(m)}(u)du$$

where $(u)_+ = u$ for $u \geq 0$ and $(u)_+ = 0$ otherwise.

Let

$$\phi_v(t) = \frac{t^{v-1}}{(v-1)!}, \quad v = 1, 2, \ldots, m$$

and $\mathcal{H}_0 = \text{span}\{\phi_1, \phi_2, \ldots, \phi_m\}$ with norm $\|\phi\|^2 = \sum_{v=0}^{m-1} [(D^{(v)}\phi)(0)]^2$, then $D^{(m)}(\mathcal{H}_0) = 0$. It has been proved in [63] that $\mathcal{H}_0$ is an RKHS with reproducing kernel $R^0(s, t) = \sum_{v=1}^{m} \phi_v(s)\phi_v(t)$. For a function $f_0 \in \mathcal{H}_0$, we can express f_0 using the basis of $\mathcal{H}_0$, i.e., $f_0(t) = \sum_{v=1}^{m} d_v \phi_v(t)$.

Let $\mathcal{B}_m$ be a set of functions satisfying boundary condition $f^{(v)}(0) = 0, v = 0, 1, 2, \ldots, m - 1$, and $G_m(t, u) = ((t - u)_+^{m-1}/(m-1)!)$, then

$$f_1(t) = \int_0^1 \frac{(t-u)_+^{m-1}}{(m-1)!} f^{(m)}(u)du = \int_0^1 G_m(t, u) f^{(m)}(u)du$$

belongs to space $\mathcal{H}_1$ defined as follows:

$$\mathcal{H}_1 = \{f : f \in \mathcal{B}_m, f, f', \ldots, f^{(m-1)} \text{ absolutely continuous,}$$
$$f^{(m)} \in \mathcal{L}_2\} \tag{3}$$

where $\mathcal{H}_1$ is a Hilbert space on [0, 1] with norm $\|f\|^2 = \int_0^1 (f^{(m)}(t))^2 dt$. $\mathcal{H}_1$ has also been proved to be an RKHS in [63] with reproducing kernel $R^1(s, t) = \int_0^1 G_m(t, u)G_m(s, u)du$. For a function $f_1 \in \mathcal{H}_1$, we can express f_1 via the basis of $\mathcal{H}_1$, denoted by $\{\xi_i\}_{i=1}^{n}$, so that $f_1(t) = \sum_{i=1}^{n} c_i \xi_i(t) = \sum_{i=1}^{n} c_i R^1(s_i, t)$, where $\xi_i = R^1(s_i, \cdot)$.

Due to

$$\int_0^1 ((D^{(m)} f_0)(u))^2 du = 0, \quad \sum_{v=0}^{m-1} ((D^{(v)} f_1)(0))^2 = 0$$

we can construct a direct sum space $\mathcal{G}_m$ by the two RKHS spaces $\mathcal{H}_0$ and $\mathcal{H}_1$, i.e., $\mathcal{G}_m = \mathcal{H}_0 \oplus \mathcal{H}_1$. $\mathcal{G}_m$ is proved as an RKHS in [63] with the following reproducing kernel:

$$R(s, t) = \sum_{v=1}^{m} \phi_v(s)\phi_v(t) + \int_0^1 G_m(t, u)G_m(s, u)du \tag{4}$$

and norm

$$\|f\|^2 = \sum_{v=0}^{m-1} [(D^{(v)} f)(0)]^2 + \int_0^1 (f^{(m)})^2(t)dt \tag{5}$$

where $f \in \mathcal{G}_m$. As a summary, for $f \in \mathcal{G}_m$, we have $f = f_0 + f_1$, with $f_0 \in \mathcal{H}_0$ and $f_1 \in \mathcal{H}_1$. It can also be written as

$$f(t) = \sum_{v=1}^{m} d_v \phi_v(t) + \sum_{i=1}^{n} c_i \xi_i(t) \tag{6}$$

where $t \in [0, 1]$.

Let $\vec{f} = (f(t_1), f(t_1), \ldots, f(t_n))'$ be the intensity values of f at $t_i \in [0, 1], i = 1, 2, \ldots, n$, and let

$$\vec{g} = \vec{f} + \eta \qquad (7)$$

be a noisy observation with η an additive Gaussian noise.

Let T be an $n \times m$ matrix with $T_{i,v} = \phi_v(t_i)$ and let Σ be an $n \times n$ matrix with $\Sigma_{i,j} = \langle \xi_i, \xi_j \rangle$, we have the relation $\vec{f} = Td + \Sigma c$, where $d = (d_1, d_2, \ldots, d_m)'$ and $c = (c_1, c_2, \ldots, c_n)'$. In [63], the following model is used to estimate $\vec{f}$ from noisy discrete measurements $\vec{g}$:

$$\min_{c,d} \frac{1}{n} \| \vec{g} - Td - \Sigma c \|^2 + \lambda c' \Sigma c \qquad (8)$$

where the second term penalties nonsmoothness.

The simple model (8) has a closed-form solution

$$c = M^{-1}(I - T(T'M^{-1}T)^{-1}T'M^{-1})\vec{g}$$
$$d = (T'M^{-1}T)^{-1}T'M^{-1}\vec{g}$$

where $M = \Sigma + n\lambda I$ with I an identity matrix. The computation burden of matrix inverse can be reduced via QR decomposition (see the details in [63, Ch. 1]).

Remark 1: Once c and d are estimated from (8), one can get an estimate for the signal function $f(x)$

$$f(x) = \sum_{v=1}^{m} d_v \phi_v(x) + \sum_{i=1}^{n} c_i \xi_i(x)$$
$$= \sum_{v=1}^{m} d_v \phi_v(x) + \sum_{i=1}^{n} c_i R^1(s_i, x) \qquad (9)$$

for any $x \in [0, 1]$.

Next, we will review 2D thin-plate spline that can be viewed as an extension of the mentioned 1D spline.

C. 2D Thin-Plate Spline and Image Smoothing

We use 2D thin-plate spline-based RKHS, introduced in [63], for image SR in this paper. We thus review it.

Similar to the 1D case, let f be the intensity function of a 2D image defined on a continuous domain $E^2 = [0, 1] \times [0, 1]$. We assume that f belongs to an RKHS. Let $\vec{f} = (f(t_1), f(t_1), \ldots, f(t_n))'$ be its discretization on grids $t_i = (x_i, y_i) \in [0, 1] \times [0, 1], i = 1, 2, \ldots, n$, the noisy image of vector form with an additive noise η can be described by

$$\vec{g} = \vec{f} + \eta. \qquad (10)$$

In [63], an optimal estimate of f for spline smoothing problems can be obtained by minimizing the following model:

$$\min \frac{1}{n} \| \vec{g} - \vec{f} \|^2 + \lambda J_m(f) \qquad (11)$$

where m is a parameter to control the total degree of polynomial, and the penalty term is defined as follows:

$$J_m(f) = \sum_{v=0}^{m} \int_{-\infty}^{+\infty} \int_{-\infty}^{+\infty} C_m^v \left(\frac{\partial^m f}{\partial x^v \partial y^{m-v}} \right)^2 dxdy. \qquad (12)$$

From [63, Ch. 2], we know that the null space of the penalty function $J_m(f)$ is an $M = C_{d+m-1}^d$-dimensional space spanned by the polynomials of degree no more than $m - 1$.

In the experiments, we let $d = 2$ (for 2D), $m = 3$, then $M = C_{d+m-1}^d = 6$, so the null space can be spanned by the following terms: $\phi_1(x, y) = 1, \phi_2(x, y) = x, \phi_3(x, y) = y, \phi_4(x, y) = xy, \phi_5(x, y) = x^2$, and $\phi_6(x, y) = y^2$. Duchon [18] has proved that if there exists $\{t_i\}_{i=1}^n$ so that least squares regression on $\{\phi_v\}_{v=1}^M$ is unique, then the optimization model (11) has a unique solution as follows:

$$f_\lambda(t) = \sum_{v=1}^{M} d_v \phi_v(t) + \sum_{i=1}^{n} c_i E_m(t, t_i) \qquad (13)$$

where $E_m(t, t_i)$ is a Green's function for the m-iterated Laplacian defined as

$$E_m(s, t) = E_m(|s - t|) = \theta_{m,d} |s - t|^{2m-d} \ln|s - t|$$

where $\theta_{m,d} = ((-1)^{d/2+m+1}/2^{2m-1}\pi^{d/2}(m-1)!(m-d/2)!)$, especially $E_m(t, t_i)$ plays the same role with $\xi_i(t)$ in the 1D case.

Similar to (8), model (11) can be rewritten as

$$\min \frac{1}{n} \| \vec{g} - (Td + Kc) \|^2 + \lambda c' Kc \qquad (14)$$

where T is an $n \times M$ matrix with $T_{i,v} = \phi_v(t_i)$ and K is an $n \times n$ matrix with $K_{i,j} = E_m(t_i, t_j)$. This model also has a similar closed-form solution with the 1D case: $d = (T'W^{-1}T)^{-1}T'W^{-1}\vec{g}$, $c = W^{-1}(I - T(T'W^{-1}T)^{-1}T'W^{-1})\vec{g}$, where $W = K + n\lambda I$. In addition, a more economical version that utilizes QR decomposition has also been provided to compute the coefficients c and d (see the details in [63]). Moreover, more information about the thin-plate spline can also be found in [16]–[18], [42], [51], and [64].

Remark 2: Once we have computed coefficients c and d, the underlying function f on the continuous domain E^2 can be estimated as

$$f(w) = \sum_{v=1}^{M} d_v \phi_v(w) + \sum_{i=1}^{n} c_i E_m(t_i, w) \qquad (15)$$

for any $w = (x, y)' \in E^2$. One thus can get an estimate of $f(w)$ at any $w \in [0, 1] \times [0, 1]$. This is very powerful and makes image SR possible.

III. PROPOSED ITERATIVE METHOD

Let f represent the intensity function of an image defined on a continuous domain. Without loss of generality, we assume that the domain is $E^2 = [0, 1] \times [0, 1]$. Let H and L be an HR and an LR discretization of f, respectively. For notation simplicity, we interchangeably use H and L to represent their matrix and vector representations. H and L are usually formulated by $L = DBH + \epsilon$ as described in (1), with D and B a downsampling and a blurring operator, respectively, and ϵ some random noise or 0 for the noise-free case. We note that the HR image $H \in \mathbb{R}^{U \times V}$ can be obtained by $H_i = f(t_i^h)$ with $t_i^h = (x_i, y_i)$, $x_i \in \{0, (1/U - 1), (2/U - 1), \ldots, 1\}$, $y_i \in \{0, (1/V - 1), (2/V - 1), \ldots, 1\}$ on a finer grid. LR image $L \in \mathbb{R}^{Q \times S}$ is gotten by the discretization formula $L_i = f(t_i^l)$ with $t_i^l = (x_i, y_i)$, $x_i \in \{0, (1/Q - 1), (2/Q - 1), \ldots, 1\}$, $y_i \in \{0, (1/S - 1), (2/S - 1), \ldots, 1\}$ on a coarser grid.

In particular, Q and S are smaller than U and V, respectively. Actually, $T^l \in \mathcal{R}^{n \times M}$, $K^l \in \mathcal{R}^{n \times n}$ and $T^h \in \mathcal{R}^{N \times M}$, $K^h \in \mathcal{R}^{N \times n}$ are the T, K matrices and $\widetilde{T}, \widetilde{K}$ matrices in Section II-C, respectively, where $n = Q \cdot S$, $N = U \cdot V$, and M is the dimension of the null space of the penalty term (also see the details in Section II-C). Motivated by the smoothing model (14), c and d can be solved using the following model:

$$\min \frac{1}{n} \|L - DB(T^h d + K^h c)\|^2 + \lambda c' K^l c \qquad (16)$$

where $H = T^h d + K^h c$.

However, model (16) is for image smoothing. The SR results via this model may smooth out image edges. In this paper, we employ Heaviside functions to recover more image details such as edges.

A. Heaviside Function

Heaviside function, or Heaviside step function [see Fig. 2(a)], is defined as follows:

$$\phi(x) = \begin{cases} 0, & x < 0 \\ 1, & x \geq 0. \end{cases} \qquad (17)$$

The Heaviside function is singular at $x = 0$ and describes a jump at $x = 0$ perfectly. We usually use its smooth approximation for practical problems. In our work, we use the following approximated Heaviside function (AHF):

$$\psi(x) = \frac{1}{2} + \frac{1}{\pi} \arctan\left(\frac{x}{\xi}\right) \qquad (18)$$

which approximates to $\phi(x)$ when $\xi \to 0$ and $\xi \in \mathcal{R}$ actually controls the smoothness. The smaller the ξ, the sharper the jump [see Fig. 2(b)].

The AHF $\psi(\cdot)$ is a 1D function. Its variation $\psi(\mathbf{v}_i \cdot \mathbf{x} + c_i)$ is, however, a 2D function when $\mathbf{x} \in \mathcal{R}^2$. If we let $\mathbf{v}_i = (\cos\theta_i, \sin\theta_i)$, $\psi(\mathbf{v}_i \cdot \mathbf{x} + c_i)$ can actually describe an edge with orientation θ_i located at a position specified by c_i. In Fig. 3, we show some examples of $\psi((\cos\theta_i, \sin\theta_i) \cdot \mathbf{z} + c_i)$. One can observe that as θ_i and c_i vary, we get edges of various orientations at different locations. Confirmed by the following theoretical foundation, we model edges in 2D images using linear combination of this type of function.

Theorem 1 (See [35]): For any positive integers m and d and any $p \in [1, \infty)$, $\text{span}_m H_d = \{\sum_{i=1}^{m} \omega_i \psi(\mathbf{v}_i \cdot \mathbf{x} + c_i)\}$, with $\omega_i \in \mathcal{R}$, $\mathbf{v}_i \in \mathcal{R}^d$, and $c_i \in \mathcal{R}$, is approximately a compact subset of $(\mathcal{L}_p([0, 1]^d), \| \cdot \|_p)$.

2D images are defined in $\mathcal{R}^2$, i.e., $d = 2$. Based on the above theorem, we model edges in 2D images using the following:

$$g(\mathbf{z}) = \sum_{j=1}^{m} \omega_j \psi((\cos\theta_j, \sin\theta_j) \cdot \mathbf{z} + c_j) \qquad (19)$$

where small $\xi = 10^{-4}$ is used in ψ, and

$$\theta_j \in \{0, \pi/12, 2\pi/12, 3\pi/12, \ldots, 23/12\pi\}$$

while $c_j \in \{0, (1/n-1), (2/n-1), \ldots, 1\}$, where n is the number of all the pixels of the LR image, and $m = kn$, where k is the number of orientations $\{\theta_j\}$.
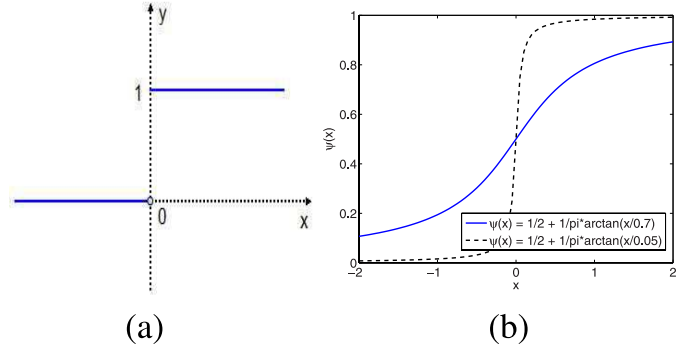

Fig. 2. (a) 1D Heaviside function. (b) Two AHFs with $\xi = 0.7$ (blue solid line) and $\xi = 0.05$ (black dashed line), respectively. The smaller the ξ, the sharper the edge. (Color images are better visualized in the pdf file.)
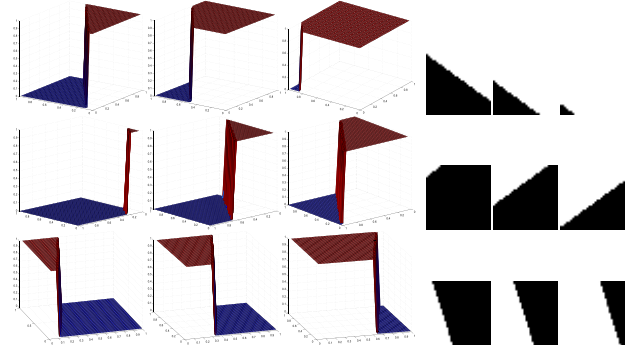

Fig. 3. Left: 3D surface images of ψ under $\xi = 10^{-4}$ and nine parameter pairs (θ, c). Right: the corresponding 2D images. From left to right and then from top to bottom: $(4\pi/5, 51/1024)$, $(4\pi/5, 25/64)$, $(4\pi/5, 175/256)$, $(6\pi/5, 135/1024)$, $(6\pi/5, 1/2)$, $(6\pi/5, 25/32)$, $(8\pi/5, 5/64)$, $(8\pi/5, 75/256)$, and $(8\pi/5, 75/128)$. (For better visualization, some 3D surface images on the left are rotated so that we can observe the edge jumps clearly.)

Actually, (19) can be written as $g = \Psi \omega$, where $\Psi \in \mathcal{R}^{n \times m}$, $g \in \mathcal{R}^n$, and $\omega \in \mathcal{R}^m$.

B. Proposed Iterative Method Based on RKHS and Heaviside Functions

In this paper, we assume that the underlying image intensity function f is the sum of smooth components and edges, which are modeled using splines-based RKHS and Heaviside functions, i.e., $f = Td + Kc + \Psi\beta$. Since Ψ contains a pretty exhaustive list of functions while edges are pretty sparse in images, it is thus reasonable to expect β to be sparse. The final proposed model is as follows:

$$\min \frac{1}{n} \|L - DB(T^h d + K^h c + \Psi^h \beta)\|^2 + \lambda c' K^l c + \alpha \|\beta\|_1 \qquad (20)$$

where $H = T^h d + K^h c + \Psi^h \beta$ and ℓ_1 sparsity is enforced for β. For the blur-free case, $B = I$, an identity matrix, $DB(T^h d + K^h c + \Psi^h \beta)$, is considered as $T^l d + K^l c + \Psi^l \beta$. Since $\|\beta\|_1$ is not differentiable, we make a variable substitution and solve the following equivalent problem:

$$\min \frac{1}{n} \|L - (T^l d + K^l c + \Psi^l \beta)\|^2 + \lambda c' K^l c + \alpha \|u\|_1$$
$$\text{s.t. } u = \beta \qquad (21)$$

using the alternating direction method of multipliers (ADMM) that is a very popular method for solving L_1 problem [29], [31], [67]. In particular, the convergence of ADMM method is guaranteed by [28] and [32]. The augmented Lagrangian of problem (21) is as follows:

$$\mathcal{L}(c, d, \beta, u) = \frac{1}{n}\|L - (T^l d + K^l c + \Psi^l \beta)\|^2 + \lambda c' K^l c$$
$$+ \alpha \|u\|_1 + \frac{\rho}{2}\|u - \beta + b\|^2 \qquad (22)$$

where α and $\rho \in \mathcal{R}$ are regularization parameters and b is a Lagrangian multiplier.

The energy functional in (22) is separable with respect to (c, d, β) and u. We can thus focus on the two subproblems

(c, d, β)-subproblem:

$$\min_{(c,d,\beta)} \frac{1}{n}\|L - (T^l d + K^l c + \Psi^l \beta)\|^2$$
$$+ \lambda c' K^l c + \frac{\rho}{2}\|u - \beta + b\|^2 \qquad (23)$$

u-subproblem: $\min_u \alpha\|u\|_1 + \frac{\rho}{2}\|u - \beta + b\|^2$. (24)

The u-subproblem (24) has a closed-form solution and is calculated for each u_i (see [67]) as

$$u_i = \text{shrink}\left(\beta_i - b_i, \frac{\alpha}{\rho}\right) \qquad (25)$$

where $\text{shrink}(a, b) = \text{sign}(a)\max(|a - b|, 0)$ and $0.(0/0) = 0$ is assumed.

We employ least squares method to solve the (c, d, β)-subproblem (23). The normal equation reads as

$$\begin{pmatrix} K^{l'}K^l + n\lambda K^l & K^{l'}T^l & K^{l'}\Psi^l \\ T^{l'}K^l & T^{l'}T^l & T^{l'}\Psi^l \\ \Psi^{l'}K^l & \Psi^{l'}T^l & \Psi^{l'}\Psi^l + \frac{n\rho}{2}I \end{pmatrix} \begin{pmatrix} c \\ d \\ \beta \end{pmatrix}$$
$$= \begin{pmatrix} K^{l'}L \\ T^{l'}L \\ \Psi^{l'}L + \frac{n\rho}{2}(u + b) \end{pmatrix}. \qquad (26)$$

Equation (26) can be rewritten as the following three equations:

$$(K^{l'}K^l + n\lambda K^l)c + K^{l'}T^l d + K^{l'}\Psi^l \beta = K^{l'}L \qquad (27)$$

$$T^{l'}K^l c + T^{l'}T^l d + T^{l'}\Psi^l \beta = T^{l'}L \qquad (28)$$

$$\Psi^{l'}K^l c + \Psi^{l'}T^l d + \left(\Psi^{l'}\Psi^l + \frac{n\rho}{2}I\right)\beta = \Psi^{l'}L + \frac{n\rho}{2}(u + b). \qquad (29)$$

We can solve for β from (29) in terms of c and d

$$\beta = \left(\Psi^{l'}\Psi^l + \frac{n\rho}{2}I\right)^{-1}$$
$$\times \left(\Psi^{l'}L + \frac{n\rho}{2}(u + b) - \Psi^{l'}K^l c - \Psi^{l'}T^l d\right). \qquad (30)$$

We then substitute (30) into (27) and (28) and obtain

$$c = \left(A_1 - A_3 A_4^{-1} A_2\right)^{-1}\left(e_1 - A_3 A_4^{-1} e_2\right)$$

$$d = A_4^{-1}(e_2 - A_2 c)$$

$$\beta = \left(\Psi^{l'}\Psi^l + \frac{n\rho}{2}I\right)^{-1}$$
$$\times \left(\Psi^{l'}L + \frac{n\rho}{2}(u + b) - \Psi^{l'}K^l c - \Psi^{l'}T^l d\right) \qquad (31)$$

Algorithm 1 ADMM Algorithm to Minimize (22)

Input: Given L, T^l, K^l, Ψ^l, λ, α, ρ, $\gamma \in (0, (\sqrt{5} + 1)/2)$
Output: c, d, β
  $j \leftarrow 0$, $(c^{(j)}, d^{(j)}, \beta^{(j)}) \leftarrow 0$, $u^{(j)} \leftarrow 0$, $b^{(j)} \leftarrow 0$
  while not converged do
    1. $j \leftarrow j + 1$
    2. $(c^{(j)}, d^{(j)}, \beta^{(j)}) \leftarrow$ solve subproblem (23) for
      $u = u^{(j-1)}$, $b = b^{(j-1)}$
    3. $u^{(j)} \leftarrow$ solve subproblem (24) for $\beta = \beta^{(j)}$,
      $b = b^{(j-1)}$
    4. $b^{(j)} \leftarrow b^{(j-1)} + \gamma\left(u^{(j)} - \beta^{(j)}\right)$
  End while.

Algorithm 2 [Single-Image Super-Resolution via RKHS (SR-RKHS)]

Input: one low-resolution image $L \in \mathbb{R}^{Q \times S}$, $\lambda > 0$, $\alpha > 0$, τ: maximum number of iteration
Output: high-resolution image $\widehat{H} \in \mathbb{R}^{U \times V}$
  Step 1. Set coarse grids t^l and fine grids t^h.
  Step 2. Construct matrices T^l, K^l, Ψ^l (refer to Sections II-C and III-A) for $i, j = 1, 2, \ldots, n$, $n = Q.S$, $\nu = 1, 2, \ldots, M$. Similarly for T^h, K^h, Ψ^h except $i = 1, 2, \ldots, N$; $j = 1, 2, \ldots, n$, where $N = U \cdot V$.
  Step 3. Initialization: $L^{(1)} = L$.
    for k = 1: τ
    a. Compute the coefficients: $(c^{(k)}, d^{(k)}, \beta^{(k)}) = \text{argmin}\frac{1}{n}\|L^{(k)} - DB(T^h d + K^h c + \Psi^h \beta)\|^2 + \lambda c' K^l c + \alpha\|\beta\|_1$.
    b. Update the high-resolution image: $H^{(k)} = T^h d^{(k)} + K^h c^{(k)} + \Psi^h \beta^{(k)}$.
    c. Downsampling $H^{(k)}$ to coarse grid: $\widetilde{L} = DBH^{(k)}$.
    d. Compute residual: $L^{(k+1)} = L^{(k)} - \widetilde{L}$.
    end
  Step 4. Compute the final high-resolution image:
    $\widehat{H} = \sum_{i=1}^{\tau} H^{(i)}$.

---

where $A_1 = (K^{l'}K^l + n\lambda K^l) - K^{l'}\Psi^l(\Psi^{l'}\Psi^l + (n\rho/2)I)^{-1}\Psi^{l'}K^l$, $A_2 = T^{l'}K^l - T^{l'}\Psi^l(\Psi^{l'}\Psi^l + (n\rho/2)I)^{-1}\Psi^{l'}K^l$, $A_3 = K^{l'}T^l - K^{l'}\Psi^l(\Psi^{l'}\Psi^l + (n\rho/2)I)^{-1}\Psi^{l'}T^l$, $A_4 = T^{l'}T^l - T^{l'}\Psi^l(\Psi^{l'}\Psi^l + (n\rho/2)I)^{-1}\Psi^{l'}T^l$, $e_1 = K^{l'}L - K^{l'}\Psi^l(\Psi^{l'}\Psi^l + (n\rho/2)I)^{-1}(\Psi^{l'}L + (n\rho/2)(u + b))$, and $e_2 = T^{l'}L - T^{l'}\Psi^l(\Psi^{l'}\Psi^l + (n\rho/2)I)^{-1}(\Psi^{l'}L + (n\rho/2)(u + b))$. Equation (31) looks complicated and involves some matrix inversions, but we compute it only once in the algorithm and the matrix inversions are not ill conditioned with proper λ and ρ. If we apply the algorithm to image patches (see the details at the end of this section), the computation is very cheap.

The following algorithm is the corresponding ADMM scheme.

Note that the convergence of Algorithm 1 is guaranteed by the following theorem that its proof can be found in [28].

Theorem 2: For any $\gamma \in (0, (\sqrt{5} + 1)/2)$, the sequence $\{(c^{(j)}, d^{(j)}, \beta^{(j)})\}$ obtained by Algorithm 1

converges to the solution of problem (20) for any initial points $u^{(0)}$ and $b^{(0)}$.

In particular, we set $\gamma = 1$ and $\beta^{(0)} = b^{(0)} = 0$ in our work, and the convergence of Algorithm 1 thus can be guaranteed.

Although model (20) can pick up more image details, it cannot completely overcome blur effect along the edges of the HR image. Due to imperfect reconstruction from the model, we observe residual edges in a difference image $L - DBH^{(1)}$, where $H^{(1)}$ is the computed HR image by model (20). Inspired by the iterative back projection method [34] and the iterative regularization method [47], we consider the difference $L - DBH^{(1)}$ as a new LR input L and recompute model (20) to get a residual HR image $H^{(2)}$. We repeat this process until the residual is small enough. The sum of the HR image $H^{(1)}$ and its residual HR images is the resulted SR image $\widehat{H}$. The strategy can recover more image details (see Fig. 4). In our experiments, it is enough to iterate the process ten times. Algorithm 2 summarizes the proposed iterative RKHS algorithm for single-image SR. This algorithm can work for general D and B though we mainly tested it with bicubic downsampling and blur free in the experiments.

For Algorithm 2, note that although we introduce some parameters in the SR algorithm, these parameters are all not sensitive and easy to select (see the remark on parameters in Section IV). The solution of step 3a is obtained by Algorithm 1. Downsampling operators D, associated with steps 3a and 3c in Algorithm 2, are done by bicubic interpolation (in MATLAB function: imresize).

Algorithm 2 can be applied to the whole image or patch by patch. In our numerical experiments, we apply the algorithm to image patches to reduce computation time and storage. We set patch size to be 6×6 with overlaps. Intensity at the boundary is estimated by bicubic interpolation.

In what follows, we compare the proposed approach with some competitive methods.

IV. NUMERICAL EXPERIMENTS

In this section, we mainly compare the proposed approach with some state-of-the-art SR methods: bicubic interpolation, a fast upsampling method (08'TOG [53]), and a learning-based method (10'TIP [71]). In addition, the proposed method can actually be viewed as an interpolation-based approach. Thus, it is necessary to compare the proposed method with some state-of-the-art interpolation methods, e.g., two contour stencils-based interpolations (11'SIAM [26] and 11'IPOL [27]) and an interpolation- and reconstruction-based method (14'TIP [65]). Furthermore, we also compare the proposed method with a kernel regression method (07'TIP [59]) and multiscale geometric method (07'SPIE [45]).

We use two kinds of test images. One is LR images without HR ground truth (see Section IV-A). The other is simulated LR images from the known HR images (see Section IV-B). In the later case, one has HR ground truth available for quantitative comparisons. For fair comparison, we set $B = I$

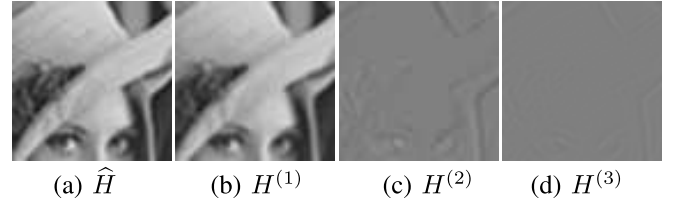(a) $\widehat{H}$ 　　 (b) $H^{(1)}$ 　　 (c) $H^{(2)}$ 　　 (d) $H^{(3)}$

Fig. 4. SR image *Lena* by Algorithm 2. (a) Sum image of $H^{(i)}$, $i = 1, 2, 3$. (b) Computed image for the first iteration. For better vision, we add 0.5 to the intensities of (c) $H^{(2)}$ and (d) $H^{(3)}$. From the last two images, we know that $H^{(2)}$ and $H^{(3)}$ pick up some image details.

in our experiments because some of the methods compared do not involve deblurring process. All the experiments are done in MATLAB (R2010a) on a laptop of 3.25-GB RAM and Intel Core i3-2370M CPU: @2.40 GHz.

The proposed algorithm (Algorithm 2) is for grayscale images. For color images such as RGB, there is redundancy in channels; we first transform it to YCbCr color space,[1] where Y represents luminance component and Cb and Cr represent blue-difference and red-difference components that are less redundant. Y is essentially a grayscale copy of the color image and carries most of the HR details of the color image. This color space is very popular in image/video processing. Because humans are more sensitive to luminance changes, the proposed algorithm is applied only to the illuminance channel and bicubic interpolation is applied to the color layers (Cb and Cr). The upscaled images in the YCbCr space are transformed back to the original color space for visualization/analysis. The color image results are better visualized in the original pdf file.

We employ root-mean-square error (RMSE) for quantitative comparisons, and the RMSE index is used in some SR works, e.g., 10'TIP [71]. Furthermore, a popular index peak signal–noise ration (PSNR) is utilized to estimate the performance of different methods. In particular, we compute PNSR only on the luminance channel Y in the experiments. In addition, we also employ the structural similarity (SSIM) index[2] [68] to compare different methods.

A Remark on Parameter Selection: The related parameters in Algorithms 1 and 2 are easy to select. We set $\lambda = 10^{-11}$, $\alpha = 10^{-4}$, and $\rho = 10^{-5}$. The maximum iteration τ is three. For simplicity, we do only ten iterations for Algorithm 1. In addition, we set $M = 6$ so that $\phi_1(t) = 1, \phi_2(t) = x$, $\phi_3(t) = y, \phi_4(t) = xy, \phi_5(t) = x^2$, and $\phi_6(t) = y^2$ (see the details in Section II-C). Note that the proposed method includes many parameters, e.g., λ, ρ, patch size, and so on. However, they are easy to select because the proposed method that can be viewed as an interpolation approach is not sensitive to the selection of parameters. Actually, choosing suitable parameters is always a difficulty to many image algorithms. Tuning empirically is a popular way to determine parameters. In our work, we obtain the parameters by tuning empirically.

---

[1] http://en.wikipedia.org/wiki/YCbCr
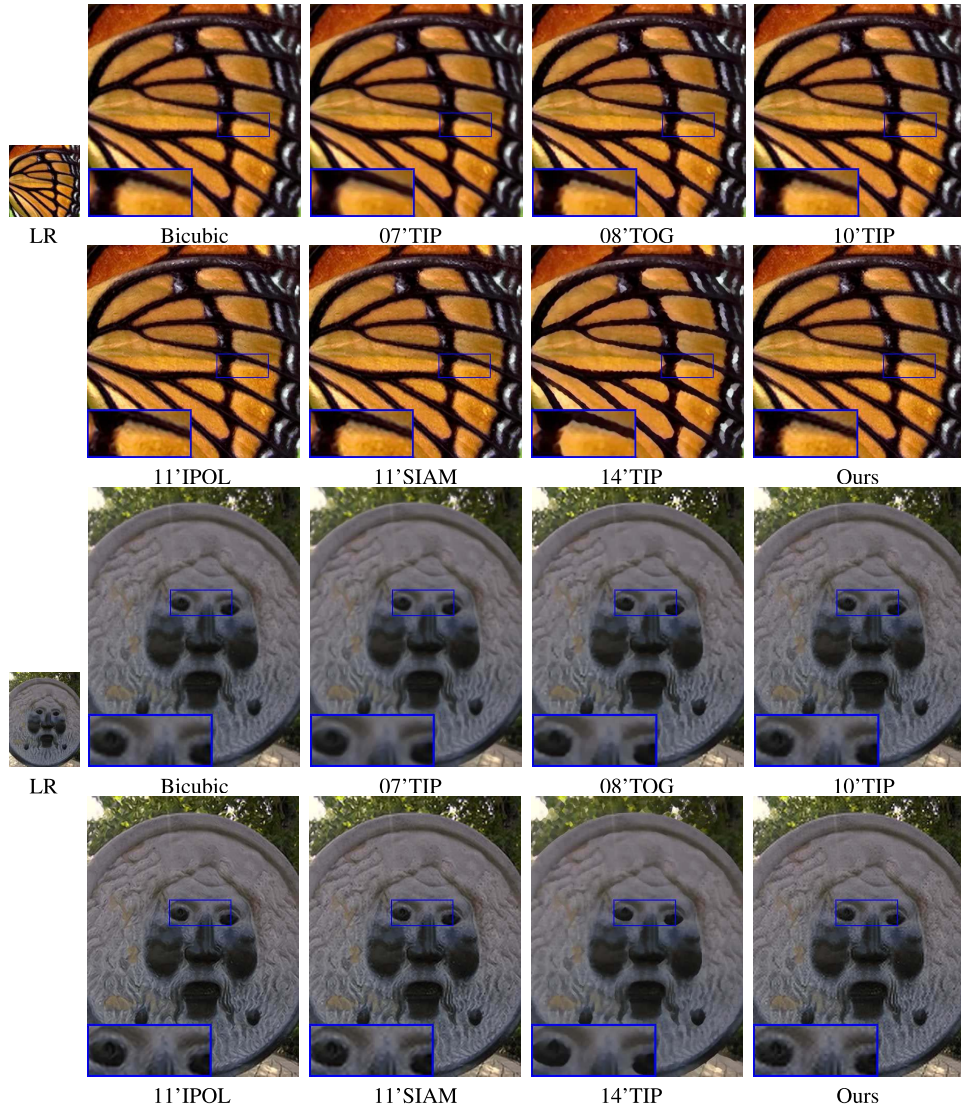[2] https://ece.uwaterloo.ca/~z70wang/research/ssim/

Fig. 5. Compare the proposed algorithm with some state-of-the-art approaches: bicubic interpolation, 07'TIP [59], 08'TOG [53], 10'TIP [71], 11'IPOL [27], 11'SIAM [26], and 14'TIP [65]. The upscaling factor is 3. No ground-truth HR images are available for quantitative comparison. Color images are better visualized in the pdf file.

A. Results on Low-Resolution Images Without Ground Truth

In this section, experiments are based on natural images without ground truth, thus quantitative comparisons (e.g., RMSE) are not available.

In Figs. 5 and 6, we compare the proposed SR-RKHS method with classical bicubic interpolation, 07'TIP [59], 08'TOG [53], 10'TIP [71], 11'IPOL [27], 11'SIAM [26], and 14'TIP [65]. The upscaling factors are all 3. From Figs. 5 and 6, the results of bicubic interpolation, 07'TIP, and 08'TOG show blur effect for the whole image. The results of 10'TIP and 14'TIP preserve sharp edges well; however, they smooth out image details on nonedge regions, e.g., freckles on the skin (see the closeups in Fig. 6). The two contour interpolation methods 11'IPOL and 11'SIAM keep image edges and details well, but the results contain some artificial contours near true edges. The proposed method performs well,

not only on edges but also for fine details/textures away from the edges.

B. Results on Low-Resolution Images Simulated From Known Ground-Truth Images

To provide quantitative comparisons in terms of RMSE, PSNR, and SSIM, we start from some HR images, treat them as ground truth, and simulate LR images by bicubic interpolation.

In this section, we mainly compare the proposed method with several state-of-the-art methods: bicubic interpolation, 08'TOG [53], 10'TIP [71], 11'IPOL [27], and 14'TIP [65]. In Figs. 7–9, upscaled HR images by bicubic interpolation show blur effect. Although we can get sharp edges via 08'TOG [53], it flattens the details on nonedge regions. The method 11'IPOL [27] recovers image details well, but introduces some artificial contours near true edges. For instance, for

Fig. 6. More examples to compare the proposed method with some state-of-the-art methods. Note that the upscaling factor is also 3.
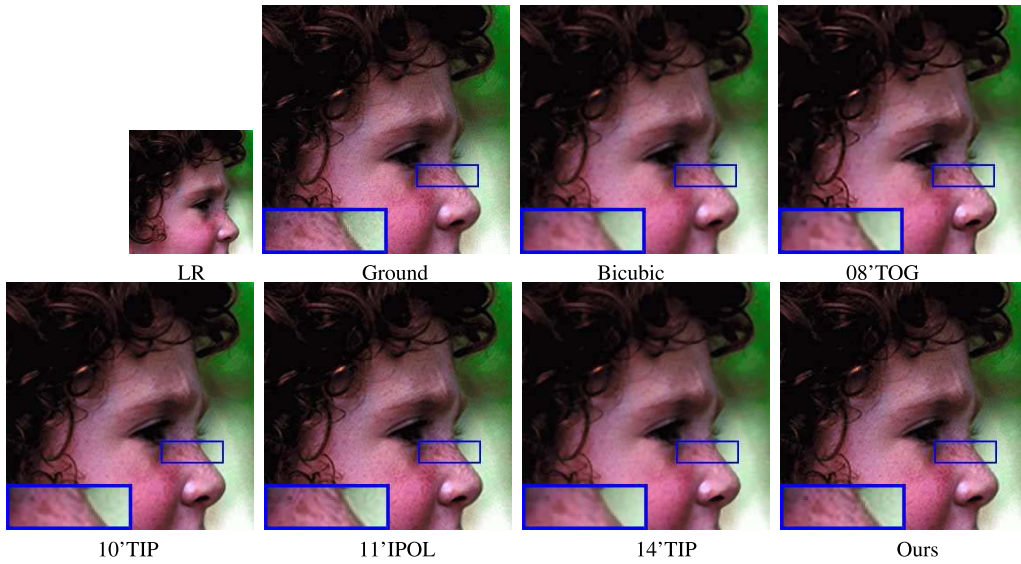

Fig. 7. Qualitative comparison for the image face among the proposed method, bicubic interpolation, 08'TOG [53], 10'TIP [71], 11'IPOL [27], and 14'TIP [65], with an upscaling factor of 2.
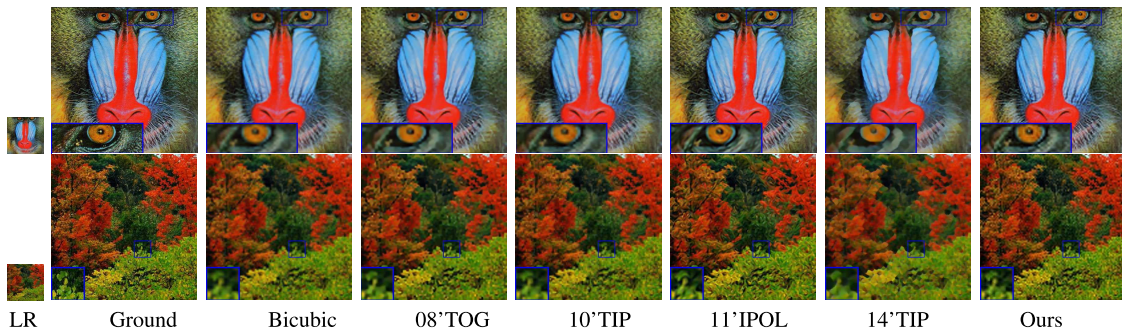

Fig. 8. Results of *Baboon* (upscaling factor 4) and *Forest* (upscaling factor 4). Compared methods: bicubic interpolation, 08'TOG [53], 10'TIP [71], 11'IPOL [27], 14'TIP [65], and ours. In particular, readers are recommended to zoom in all the figures for better visualization.

the *Baboon* example in Fig. 8, it has many artificial contours near the true edges (see the closeup in Fig. 8). 14'TIP [65] preserves sharp image edges, but smoothes out image intensity not on edges. The method 10'TIP [71] obtains competitive visual results; however, it generates worse quantitative results than the proposed method (see Table I). In addition, the results

TABLE I

QUANTITATIVE COMPARISONS OF DIFFERENT METHODS IN TERMS OF RMSE, PSNR, AND SSIM (BOLD: THE BEST ONE
AND UNDERLINE: THE SECOND BEST). COMPARED METHODS: BICUBIC INTERPOLATION, 08'TOG [53],
10'TIP [71], 11'IPOL [27], 14'TIP [65], AND THE PROPOSED METHOD

| Image(factor)	Index	Bicubic	08'TOG	10'TIP	11'IPOL	14'TIP	Proposed
face(X2)	RMSE	4.61	5.02	4.41	_4.38_	5.55	**4.26**
	PSNR	34.86	34.11	35.24	_35.30_	33.25	**35.53**
	SSIM	0.862	0.843	0.873	_0.879_	0.828	**0.883**
baboon(X4)	RMSE	19.47	19.29	19.32	_19.22_	19.51	**19.13**
	PSNR	22.25	22.31	22.30	_22.41_	21.88	**22.43**
	SSIM	0.704	0.714	0.718	**0.760**	0.711	_0.756_
forest(X4)	RMSE	18.63	18.30	18.47	_18.44_	18.84	**18.09**
	PSNR	22.78	22.93	22.85	_22.86_	22.79	**23.03**
	SSIM	0.685	0.701	0.701	_0.738_	0.646	**0.748**
baby(X2)	RMSE	3.58	4.32	3.40	_3.37_	4.19	**3.17**
	PSNR	37.06	35.43	37.51	_37.58_	36.82	**38.19**
	SSIM	0.993	0.982	_0.995_	**0.997**	0.985	**0.997**
dog(X3)	RMSE	9.15	9.24	_9.09_	9.11	9.99	**9.02**
	PSNR	28.90	28.82	_28.96_	28.94	28.14	**29.04**
	SSIM	0.914	0.904	0.920	_0.927_	0.893	**0.928**
field(X3)	RMSE	12.49	12.32	12.27	_12.22_	13.74	**12.06**
	PSNR	26.20	26.32	26.36	_26.39_	25.37	**26.51**
	SSIM	0.600	0.595	0.615	_0.638_	0.559	**0.641**
lion(X3)	RMSE	11.03	10.66	10.67	_10.30_	11.58	**10.25**
	PSNR	27.28	27.58	27.57	_27.87_	27.13	**27.89**
	SSIM	0.883	0.894	_0.897_	**0.916**	0.874	**0.916**
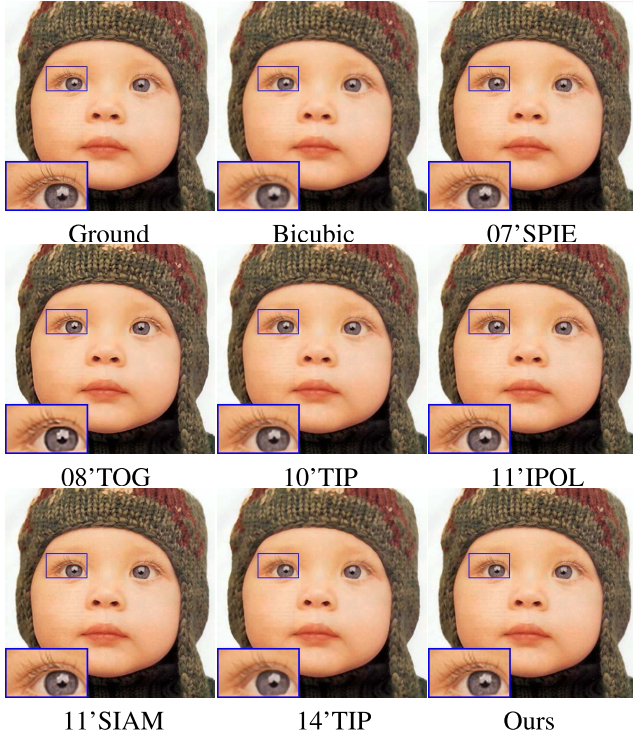
Fig. 9. Results of *Baby* with an upscaling factor of 2. First row: ground-truth image, bicubic interpolation (RMSE = 3.58; PSNR = 37.06; SSIM = 0.993), and 07'SPIE [45] (3.73; 36.70; 0.996). Second row: 08'TOG [53] (4.32; 35.43; 0.982), 10'TIP [71] (3.40; 37.51; 0.995), and 11'IPOL [27] (3.37; 37.58; 0.997). Third row: 11'SIAM [26] (3.24; 37.93; 0.997), 14'TIP [65] (4.19; 36.82; 0.985), and the proposed method (3.17; 38.19; 0.997).

method also gets the best RMSE, PSNR, and SSIM for almost all the examples.

In Fig. 10 and Table I, we find that the proposed method gets better quantitative and visual results. The results of bicubic interpolation and 08'TOG show significant blur effect. The method 11'IPOL also obtains excellent visual results, but the visual results show obvious artificial contours. The method 14'TIP gets the sharpest image edges, but it smoothes out image details on nonedge regions. In addition, the method 10'TIP obtains similarly visual results with the proposed method, but the proposed method has lower RMSE and larger PSNR and SSIM. In Fig. 11, the proposed method performs best, especially for image details, e.g., hair of *Lion*. The learning-based method 10'TIP [71] obtains excellent visual and quantitative results; it, however, needs extra training data to generate dictionary. We also give the corresponding error maps in Fig. 12. Furthermore, we can find more quantitative comparisons in Table I. It demonstrates that the proposed method gets better quantitative performance than other methods for almost all the examples. In particular, instead of RKHS and Heaviside functions, one can use wavelet basis or frames in our framework. We have not got time to compare the performance.

Computation Issue: We present the computation comparisons in Table II. From Table II, we find that bicubic interpolation is the fastest. However, we have to note that bicubic interpolation is optimized in MATLAB, 08'TOG is optimized by an executable software,[3] and 11'IPOL[4] and 14'TIP[5] are speeded up via C language and Cmex, respectively. Only 10'TIP[6] and the proposed method are based on

of 07'SPIE [45] and 11'SIAM [26] in Fig. 9 also perform worse than the proposed method. The proposed method not only preserves sharp edges but also keeps high-frequency details well on nonedge regions. Furthermore, the proposed

[3]http://www.cse.cuhk.edu.hk/~leojia/projects/upsampling/index.html
[4]http://www.ipol.im/pub/art/2011/g_iics/
[5]http://www.escience.cn/people/LingfengWang/publication.html
[6]http://www.ifp.illinois.edu/~jyang29/ScSR.htm

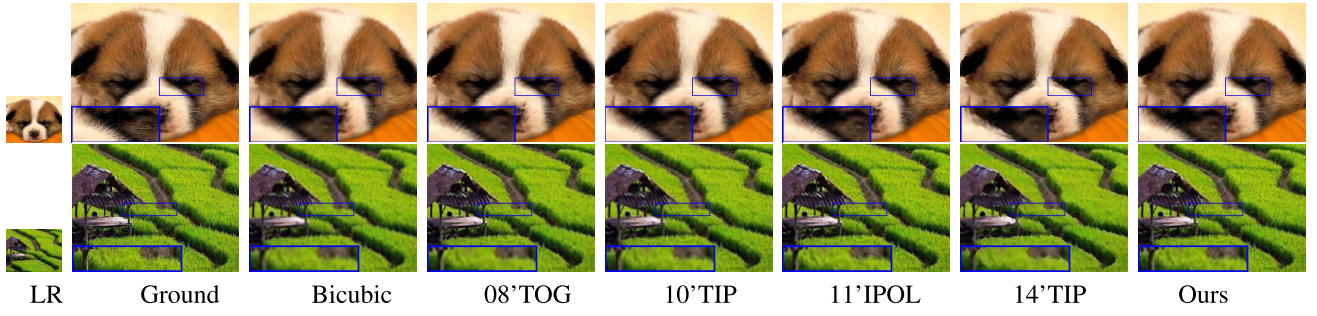| LR | Ground | Bicubic | 08'TOG | 10'TIP | 11'IPOL | 14'TIP | Ours |

Fig. 10. Results of *Dog* (upscaling factor 3) and *Field* (upscaling factor 3). Compared methods: bicubic interpolation, 08'TOG [53], 10'TIP [71], 11'IPOL [27], 14'TIP [65], and the proposed method.
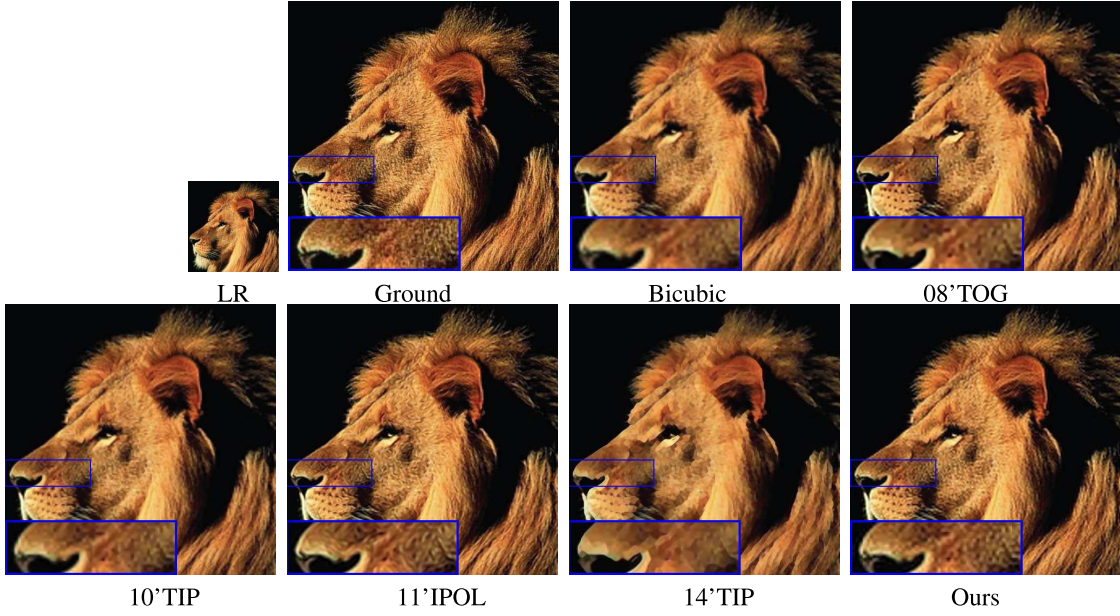

Fig. 11. Results of *Lion* with an upscaling factor of 3. Compared methods: bicubic interpolation, 08'TOG [53], 10'TIP [71], 11'IPOL [27], 14'TIP [65], and the proposed method.
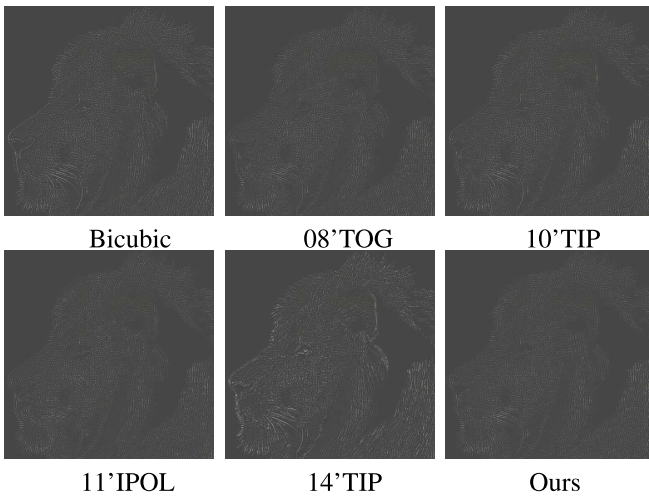

Fig. 12. Compare error maps of the proposed method and five other methods. The test image is *Lion*. The error maps are brightened for better visualization.

MATLAB codes that are not optimized. In particular, computation time with respect to the change of upscaling factor and image size is shown in Fig. 13. One can observe

that it is acceptable to employ our method for image SR. The computation time is based on nonoptimized MATLAB code. It has a lot of room to speed up the code. For instance, the code contains a lot of loops that can be significantly sped up using Cmex.

Relation Between Model (20) and Model (20) Combined With Iterative Strategy: Equation (20) is the proposed model in this paper. In particular, we employ an iterative strategy for the proposed model to recover more image details. Thus, it is necessary to illustrate the relation between model (20) and model (20) combined with our iterative strategy. Actually, there is no significant visual difference between the two methods, especially in image details and edges [see the almost dark error map in Fig. 14(c)]. However, it is easy to know that the proposed model (20) combined with the iterative strategy performs lower RMSE compared with the proposed model (20). In addition, the iterative strategy results in more computation obviously.

V. CONCLUSION

Given an LR image, the SR problem was casted as an image intensity function estimation problem. Because images

TABLE II

TIME COMPARISON OF DIFFERENT METHODS (BOLD: THE BEST ONE AND UNDERLINE: THE SECOND BEST). COMPARED
METHODS: BICUBIC INTERPOLATION, 08'TOG [53], 10'TIP [71], 11'IPOL [27], 14'TIP [65], AND THE
PROPOSED METHOD. NOTE THAT BICUBIC IS OPTIMIZED IN MATLAB, 08'TOG IS OPTIMIZED BY AN
EXECUTABLE SOFTWARE, AND 11'IPOL AND 14'TIP ARE SPEEDED UP VIA C LANGUAGE
AND CMEX, RESPECTIVELY. ONLY 10'TIP AND THE PROPOSED METHOD ARE BASED
ON MATLAB CODES THAT ARE NOT OPTIMIZED (UNIT: SECONDS)

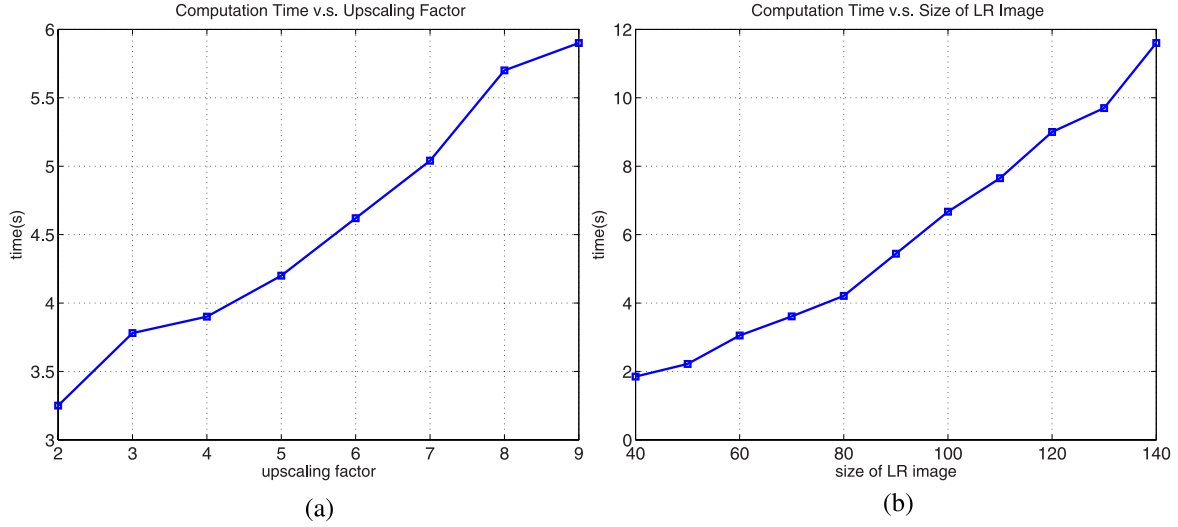| Image(factor)	size of LR	Bicubic	08'TOG	10'TIP	11'IPOL	14'TIP	Proposed
face(X2)	140×140	**0.01**	3.32	40.70	<u>0.09</u>	0.93	9.54
baboon(X4)	120×120	**0.02**	9.11	145.76	<u>0.26</u>	1.10	8.20
tree(X4)	110×110	**0.02**	5.42	115.16	<u>0.23</u>	1.03	7.74
baby(X2)	256×256	**0.05**	13.39	144.67	<u>0.37</u>	1.00	43.59
dog(X3)	130×140	**0.03**	11.00	100.32	<u>0.19</u>	0.81	12.61
field(X3)	100×133	**0.02**	9.00	81.54	<u>0.14</u>	0.67	9.65
lion(X2)	168×168	**0.03**	13.98	126.49	<u>0.25</u>	0.86	13.75

Fig. 13. (a) Computation time versus upscaling factor for LR image with size 80×80. (b) Computation time versus size of LR image. The size of the LR image is from 40×40 to 140×140, and the upscaling factor is always 5.
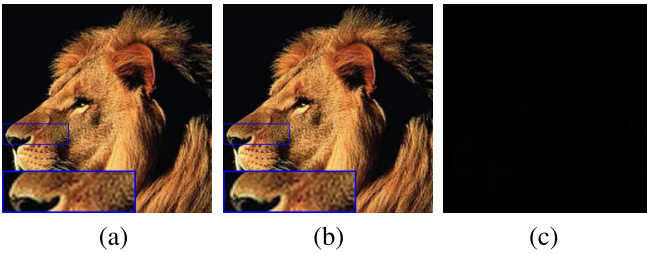

Fig. 14. (a) Result of model (20) with the iterative strategy (i.e., $\tau = 3$ in Algorithm 2 and RMSE = 10.25). (b) Result of model (20) without the iterative strategy (i.e., $\tau = 1$ in Algorithm 2 and RMSE = 10.36). (c) Error map between (a) and (b). Upscaling factor: 3.

mainly contain smooth components and edges, we assumed that smooth components belong to 2D thin-plate spline-based RKHS and edges can be represented by AHFs. The coefficients of the redundant basis were computed using the LR image. We then applied the coefficients to generate HR images. To recover sharp HR images, we proposed an iterative scheme to preserve more image details. In addition, we applied the proposed method to image patches to reduce computation

and storage significantly. Many experiments showed that the proposed approach outperformed the state-of-the-art methods, both visually and quantitatively.

REFERENCES

[1] C. B. Atkins, C. A. Bouman, and J. P. Allebach, "Tree-based resolution synthesis," in *Proc. Int. Conf. Image Process. (ICIP)*, 1999, pp. 405–410.
[2] C. B. Atkins, C. A. Bouman, and J. P. Allebach, "Optimal image scaling using pixel classification," in *Proc. Int. Conf. Image Process. (ICIP)*, 2001, pp. 864–867.
[3] S. Borman and R. L. Stevenson, "Super-resolution from image sequences—A review," in *Proc. Midwest Symp. Circuits Syst.*, Aug. 1998, pp. 374–378.
[4] P. Bouboulis, K. Slavakis, and S. Theodoridis, "Adaptive kernel-based image denoising employing semi-parametric regularization," *IEEE Trans. Image Process.*, vol. 19, no. 6, pp. 1465–1479, Jun. 2010.
[5] E. J. Candès and C. Fernandez-Granda, "Towards a mathematical theory of super-resolution," *Commun. Pure Appl. Math.*, vol. 67, no. 6, pp. 906–956, Jun. 2014.
[6] D. Capel and A. Zisserman, "Super-resolution enhancement of text image sequences," in *Proc. 15th Int. Conf. Pattern Recognit. (ICPR)*, vol. 1. 2000, pp. 600–605.
[7] A. Caponnetto, C. A. Micchelli, M. Pontil, and Y. Ying, "Universal multi-task kernels," *J. Mach. Learn. Res.*, vol. 9, pp. 1615–1646, Jul. 2008.
[8] C. Carmeli, E. De Vito, and A. Toigo, "Vector valued reproducing kernel Hilbert spaces of integrable functions and Mercer theorem," *Anal. Appl.*, vol. 4, no. 4, pp. 377–408, 2006.

[9] A. Chambolle and T. Pock, "A first-order primal-dual algorithm for convex problems with applications to imaging," *J. Math. Imag. Vis.*, vol. 40, no. 1, pp. 120–145, 2011.

[10] H. Chang, D.-Y. Yeung, and Y. Xiong, "Super-resolution through neighbor embedding," in *Proc. IEEE Comput. Soc. Conf. Comput. Vis. Pattern Recognit. (CVPR)*, vol. 1. Jun./Jul. 2004, p. 1.

[11] P. Chatterjee, S. Mukherjee, S. Chaudhuri, and G. Seetharaman, "Application of Papoulis–Gerchberg method in image super-resolution and inpainting," *Comput. J.*, vol. 52, no. 1, pp. 80–89, 2009.

[12] R. R. Coifman and S. Lafon, "Geometric harmonics: A novel tool for multiscale out-of-sample extension of empirical functions," *Appl. Comput. Harmon. Anal.*, vol. 21, no. 1, pp. 31–52, 2006.

[13] F. Cucker and S. Smale, "On the mathematical foundations of learning," *Bull. Amer. Math. Soc.*, vol. 39, no. 1, pp. 1–49, Oct. 2001.

[14] D. Glasner, S. Bagon, and M. Irani, "Super-resolution from a single image," in *Proc. IEEE 12th ICCV*, Sep./Oct. 2009, pp. 349–356.

[15] W. Dong, G. Shi, L. Zhang, and X. Wu, "Super-resolution with nonlocal regularized sparse representation," *Proc. SPIE*, vol. 7744, p. 77440H, Jul. 2010.

[16] J. Duchon, "Fonctions splines et vecteurs aléatoires," Séminaire d'Analyse Numérique, Univ. Sci. Médicale, Grenoble, France, Tech. Rep. 213, 1975.

[17] J. Duchon "Fonctions-spline et esperances conditionnelles de champs gaussiens," *Ann. Sci. l'Univ. Clermont. Math.*, vol. 61, no. 14, pp. 19–27, 1976.

[18] J. Duchon, "Splines minimizing rotation-invariant semi-norms in Sobolev spaces," in *Constructive Theory of Functions of Several Variables*. Berlin, Germany: Springer-Verlag, 1977, pp. 85–100.

[19] S. Farsiu, M. D. Robinson, M. Elad, and P. Milanfar, "Fast and robust multiframe super resolution," *IEEE Trans. Image Process.*, vol. 13, no. 10, pp. 1327–1344, Oct. 2004.

[20] R. Fattal, "Image upsampling via imposed edge statistics," *ACM Trans. Graph.*, vol. 26, no. 3, 2007, Art. ID 95.

[21] C. Fernandez-Granda and E. J. Candès, "Super-resolution via transform-invariant group-sparse regularization," in *Proc. IEEE ICCV*, Dec. 2013, pp. 3336–3343.

[22] G. Freedman and R. Fattal, "Image and video upscaling from local self-examples," *ACM Trans. Graph.*, vol. 30, no. 2, 2011, Art. ID 12.

[23] W. T. Freeman, T. R. Jones, and E. C. Pasztor, "Example-based super-resolution," *IEEE Comput. Graph. Appl.*, vol. 22, no. 2, pp. 56–65, Mar./Apr. 2002.

[24] W. T. Freeman and E. C. Pasztor, "Markov networks for super-resolution," in *Proc. 34th Annu. Conf. Inf. Sci. Syst.*, 2000.

[25] W. T. Freeman, E. C. Pasztor, and O. T. Carmichael, "Learning low-level vision," *Int. J. Comput. Vis.*, vol. 40, no. 1, pp. 25–47, 2000.

[26] P. Getreuer, "Contour stencils: Total variation along curves for adaptive image interpolation," *SIAM J. Imag. Sci.*, vol. 4, no. 3, pp. 954–979, 2011.

[27] P. Getreuer, "Image interpolation with contour stencils," *Image Process. Line*, vol. 1, Aug. 2011.

[28] R. Glowinski and P. Le Tallec, *Augmented Lagrangian and Operator-Splitting Methods in Nonlinear Mechanics*. Philadelphia, PA, USA: SIAM, 1989.

[29] T. Goldstein and S. Osher, "The split Bregman method for L1-regularized problems," *SIAM J. Imag. Sci.*, vol. 2, no. 2, pp. 323–343, 2009.

[30] E. Gur and Z. Zalevsky, "Single image digital super resolution: A revised Gerchberg–Papoulis algorithm," *IAENG Int. J. Comput. Sci.*, vol. 34, no. 2, pp. 251–255, 2007.

[31] B. He, M. Tao, and X. Yuan, "Alternating direction method with Gaussian back substitution for separable convex programming," *SIAM J. Optim.*, vol. 22, no. 2, pp. 313–340, 2012.

[32] B. He and H. Yang, "Some convergence properties of a method of multipliers for linearly constrained monotone variational inequalities," *Oper. Res. Lett.*, vol. 23, nos. 3–5, pp. 151–161, 1998.

[33] L. He, H. Qi, and R. Zaretzki, "Beta process joint dictionary learning for coupled feature spaces with application to single image super-resolution," in *Proc. IEEE Conf. CVPR*, Jun. 2013, pp. 345–352.

[34] M. Irani and S. Peleg, "Super resolution from image sequences," in *Proc. 10th Int. Conf. Pattern Recognit. (ICPR)*, Jun. 1990, pp. 115–120.

[35] P. C. Kainen, V. Kůrková, and A. Vogt, "Best approximation by linear combinations of characteristic functions of half-spaces," *J. Approx. Theory*, vol. 122, no. 2, pp. 151–159, 2003.

[36] S. H. Kang, B. Shafei, and G. Steidl, "Supervised and transductive multi-class segmentation using *p*-Laplacians and RKHS methods," *J. Vis. Commun. Image Represent.*, vol. 25, no. 5, pp. 1136–1148, Jul. 2014.

[37] J. B. Ra, C. Kim, K. Choi, and K. Hwang, "Learning-based super-resolution using a multi-resolution wavelet approach," in *Proc. Int. Workshop Adv. Image Technol. (IWAIT)*, 2009.

[38] C. Kim, K. Choi, and J. B. Ra, "Improvement on learning-based super-resolution by adopting residual information and patch reliability," in *Proc. 16th IEEE Int. Conf. Image Process. (ICIP)*, Nov. 2009, pp. 1197–1200.

[39] K. Komatsu, T. Igarashi, K. Aizawa, and T. Saito, "Very high resolution imaging scheme with multiple different-aperture cameras," *Signal Process., Image Commun.*, vol. 5, nos. 5–6, pp. 511–526, 1993.

[40] X. Li and M. T. Orchard, "New edge-directed interpolation," *IEEE Trans. Image Process.*, vol. 10, no. 10, pp. 1521–1527, Oct. 2001.

[41] V. K. Ananthashayana, "Super resolution blind reconstruction of low resolution images using wavelets based fusion," *Int. J. Comput., Inf., Syst. Sci.*, vol. 2, no. 2, pp. 105–110, 2008.

[42] J. Meinguet, "Multivariate interpolation at arbitrary points made simple," *J. Appl. Math. Phys.*, vol. 30, no. 2, pp. 292–304, 1979.

[43] J. Mercer, "Functions of positive and negative type, and their connection with the theory of integral equations," *Philos. Trans. Roy. Soc. London, A, Containing Papers Math. Phys. Character*, vol. 209, pp. 415–446, May 1909.

[44] C. A. Micchelli and M. Pontil, "On learning vector-valued functions," *Neural Comput.*, vol. 17, no. 1, pp. 177–204, 2005.

[45] N. Mueller, Y. Lu, and M. N. Do, "Image interpolation using multiscale geometric representations," *Proc. SPIE*, vol. 6498, p. 64980A, Feb. 2007.

[46] A. Nosedal-Sanchez, C. B. Storlie, T. C. M. Lee, and R. Christensen, "Reproducing kernel Hilbert spaces for penalized regression: A tutorial," *Amer. Statist.*, vol. 66, no. 1, pp. 50–60, 2012.

[47] S. Osher, M. Burger, D. Goldfarb, J. Xu, and W. Yin, "An iterative regularization method for total variation-based image restoration," *Multiscale Model. Simul.*, vol. 4, no. 2, pp. 460–489, 2005.

[48] S. C. Park, M. K. Park, and M. G. Kang, "Super-resolution image reconstruction: A technical overview," *IEEE Signal Process. Mag.*, vol. 20, no. 3, pp. 21–36, May 2003.

[49] M. H. Quang, S. H. Kang, and T. M. Le, "Image and video colorization using vector-valued reproducing kernel Hilbert spaces," *J. Math. Imag. Vis.*, vol. 37, no. 1, pp. 49–65, 2010.

[50] B. Schölkopf and A. J. Smola, *Learning With Kernels: Support Vector Machines, Regularization, Optimization, and Beyond*. Cambridge, MA, USA: MIT Press, 2002.

[51] R. S. Seaman and M. F. Hutchinson, "Comparative real data tests of some objective analysis methods by withholding observations," *Austral. Meteorological Mag.*, vol. 33, pp. 37–46, Jan. 1985.

[52] A. J. Shah and S. B. Gupta, "Image super resolution—A survey," in *Proc. 1st Int. Conf. Emerg. Technol. Trends Electron., Commun., Netw.*, Dec. 2012, pp. 1–6.

[53] Q. Shan, Z. Li, J. Jia, and C.-K. Tang, "Fast image/video upsampling," *ACM Trans. Graph.*, vol. 27, no. 5, 2008, Art. ID 153.

[54] J. Shawe-Taylor and N. Cristianini, *Kernel Methods for Pattern Analysis*. Cambridge, U.K.: Cambridge Univ. Press, 2004.

[55] J. Sun, J. Sun, Z. Xu, and H.-Y. Shum, "Image super-resolution using gradient profile prior," in *Proc. IEEE Conf. CVPR*, Jun. 2008, pp. 1–8.

[56] J. Sun, N.-N. Zheng, H. Tao, and H.-Y. Shum, "Image hallucination with primal sketch priors," in *Proc. IEEE Comput. Soc. Conf. Comput. Vis. Pattern Recognit. (CVPR)*, vol. 2. Jun. 2003, pp. II-729–II-736.

[57] S.-C. Tai, T.-M. Kuo, C.-H. Iao, and T.-W. Liao, "A fast algorithm for single image super resolution in both wavelet and spatial domain," in *Proc. Int. Symp. Comput., Consum., Control*, Jun. 2012, pp. 702–705.

[58] Y.-W. Tai, S. Liu, M. S. Brown, and S. Lin, "Super resolution using edge prior and single image detail synthesis," in *Proc. IEEE Conf. CVPR*, Jun. 2010, pp. 2400–2407.

[59] H. Takeda, S. Farsiu, and P. Milanfar, "Kernel regression for image processing and reconstruction," *IEEE Trans. Image Process.*, vol. 16, no. 2, pp. 349–366, Feb. 2007.

[60] M. F. Tappen, B. C. Russell, and W. T. Freeman, "Exploiting the sparse derivative prior for super-resolution and image demosaicing," in *Proc. IEEE Workshop Statist. Comput. Theories Vis.*, 2003.

[61] J. D. van Ouwerkerk, "Image super-resolution survey," *Image Vis. Comput.*, vol. 24, no. 10, pp. 1039–1052, 2006.

[62] F. Viola, A. Fitzgibbon, and R. Cipolla, "A unifying resolution-independent formulation for early vision," in *Proc. IEEE Conf. CVPR*, Jun. 2012, pp. 494–501.

[63] G. Wahba, *Spline Models for Observational Data* (CBMS-NSF Regional Conference Series in Applied Mathematics), vol. 59. Philadelphia, PA, USA: SIAM, 1990.

[64] G. Wahba and J. Wendelberger, "Some new mathematical methods for variational objective analysis using splines and cross validation," *Monthly Weather Rev.*, vol. 108, no. 8, pp. 1122–1145, 1980.

[65] L. Wang, H. Wu, and C. Pan, "Fast image upsampling via the displacement field," *IEEE Trans. Image Process.*, vol. 23, no. 12, pp. 5123–5135, Dec. 2014.

[66] L. Wang, S. Xiang, G. Meng, H. Wu, and C. Pan, "Edge-directed single-image super-resolution via adaptive gradient magnitude self-interpolation," *IEEE Trans. Circuits Syst. Video Technol.*, vol. 23, no. 8, pp. 1289–1299, Aug. 2013.

[67] Y. Wang, J. Yang, W. Yin, and Y. Zhang, "A new alternating minimization algorithm for total variation image reconstruction," *SIAM J. Imag. Sci.*, vol. 1, no. 3, pp. 248–272, 2008.

[68] Z. Wang, A. C. Bovik, H. R. Sheikh, and E. P. Simoncelli, "Image quality assessment: From error visibility to structural similarity," *IEEE Trans. Image Process.*, vol. 13, no. 4, pp. 600–612, Apr. 2004.

[69] X. Qinlan, C. Hong, and C. Huimin, "Improved example-based single-image super-resolution," in *Proc. 3rd Int. Congr. Image Signal Process. (CISP)*, vol. 3. Oct. 2010, pp. 1204–1207.

[70] J. Yang, Z. Wang, Z. Lin, S. Cohen, and T. Huang, "Coupled dictionary training for image super-resolution," *IEEE Trans. Image Process.*, vol. 21, no. 8, pp. 3467–3478, Aug. 2011.

[71] J. Yang, J. Wright, T. S. Huang, and Y. Ma, "Image super-resolution via sparse representation," *IEEE Trans. Image Process.*, vol. 19, no. 11, pp. 2861–2873, Nov. 2010.

[72] J. Yang, J. Wright, T. Huang, and Y. Ma, "Image super-resolution as sparse representation of raw image patches," in *Proc. IEEE Conf. Comput. Vis. Pattern Recognit. (CVPR)*, Jun. 2008, pp. 1–8.

[73] R. Zeyde, M. Elad, and M. Protter, "On single image scale-up using sparse-representations," in *Curves and Surfaces* (Lecture Notes in Computer Science), vol. 6920. Berlin, Germany: Springer-Verlag, 2012, pp. 711–730.

[74] L. Zhang and X. Wu, "An edge-guided image interpolation algorithm via directional filtering and data fusion," *IEEE Trans. Image Process.*, vol. 15, no. 8, pp. 2226–2238, Aug. 2006.

[75] Y. Zhao, J. Yang, Q. Zhang, S. Lin, Y. Cheng, and Q. Pan, "Hyperspectral imagery super-resolution by sparse representation and spectral regularization," *EURASIP J. Adv. Signal Process.*, vol. 2011, p. 87, Dec. 2011.

[76] H. Zheng, A. Bouzerdoum, and S. L. Phung, "Wavelet based nonlocal-means super-resolution for video sequences," in *Proc. 17th IEEE Int. Conf. Image Process. (ICIP)*, Sep. 2010, pp. 2817–2820.
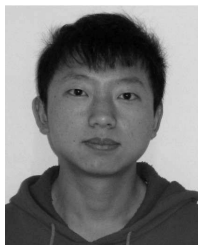
Liang-Jian Deng received the B.S. degree from the School of Mathematical Sciences, University of Electronic Science and Technology of China, Chengdu, China, in 2010, where he is currently pursuing the Ph.D. degree with the School of Mathematical Sciences.

His current research interests include image processing, including image superresolution, deblurring and denoising, inpainting, and dehazing.

Weihong Guo received the B.S. degree in computational mathematics from the Minzu University of China, Beijing, China, in 1999, and the M.S. degree in statistics and the Ph.D. degree in applied mathematics from the University of Florida, Gainesville, FL, USA, in 2007.

She was a Mathematics Assistant Professor with the University of Alabama, Tuscaloosa, AL, USA, from 2007 to 2009. She is currently an Applied Mathematics Associate Professor with Case Western Reserve University, Cleveland, OH, USA. Her current research interests include variational image reconstruction, image superresolution, and image segmentation.

Ting-Zhu Huang is currently a Professor with the School of Mathematical Sciences, University of Electronic Science and Technology of China, Chengdu, China. He received the B.S. degree, the M.S. degree, and the Ph.D. degree from Xi'an Jiaotong University, Xi'an, China, in 1986, 1992, and 2001, respectively. His current research interests include numerical linear algebra and scientific computation with applications in electromagnetics, modeling, and algorithms for image processing. He has authored over 100 papers in international journals, including the *SIAM Journal on Scientific Computing*, the *SIAM Journal on Matrix Analysis and Applications*, the *IMA Journal of Numerical Analysis*, the *Journal of Computational Physics*, *Computer Physics Communications*, *Numerical Linear Algebra with Applications*, *Automatica*, the IEEE TRANSACTIONS ON ANTENNAS AND PROPAGATION, the IEEE TRANSACTIONS ON GEOSCIENCE AND REMOTE SENSING, *Information Sciences*, the *Journal of the Optical Society of America A*, *Computing*, *Linear Algebra and its Applications*, *Applied Mathematics Letters*, *Computers and Mathematics with Applications*, *Applied Mathematical Modelling*, the *Journal of The Franklin Institute*, the *Journal of Computational and Applied Mathematics*, and *Communications in Nonlinear Science and Numerical Simulation*.

Dr. Huang received the Science and Technology Progress Award of Sichuan Province from the Chinese Information Ministry for several times. He has served on the Editorial Board of several international journals.